

DISCRETE NUMERICAL ANALYSES OF GRAIN SIZE INFLUENCE ON THE FRACTURE OF NOTCHED ROCK BEAMS

J. Justo^{a*}, H. Konietzky^b, J. Castro^a

^aGroup of Geotechnical Engineering, Universidad de Cantabria, E.T.S de Ingenieros de Caminos, Canales y Puertos, Av/ Los Castros 44, 39005, Santander, Spain

^bGeotechnical Institute, TU Bergakademie Freiberg, Gebirgs- und Felsmechanik/Felsbau, Gustav-Zeuner-Str. 1, 09599, Freiberg, Germany

* Contact person: justoj@unican.es

ABSTRACT

This paper studies the influence of the grain size and the notch effect on the fracture assessment of U-shaped notched rock beams through the variation of the apparent fracture toughness. The research is based on an exhaustive campaign that comprises numerical simulations of 300 four-point bending tests, 30 simple compression tests and 60 tensile splitting (Brazilian) tests. Non-porous, isotropic ideal and equivalent rocks with 5 different uniform grain sizes are modelled using the distinct element method, where the rocks are modelled as a discontinuous material, defining explicitly the grains and the boundary conditions. Several notch radii are simulated and the corresponding variation in the apparent fracture toughness is observed. This notch effect is interpreted using the Theory of Critical Distances (TCD), which uses a material intrinsic property called the critical distance (L) to evaluate the stress field around the notch tip. The paper shows the variation of the fundamental rock properties with the grain size, the applicability of the TCD to evaluate the notch effect and the correlation between the critical distance and the grain size.

Keywords: Grain size; Rock; Fracture; Notch; TCD; DEM

1. INTRODUCTION

Rock fracture is of interest in many engineering fields such as underground engineering (e.g., tunnelling, mining) or energy engineering (e.g., gas-oil extractions, geothermal energy). The presence of stress risers, such as defects, cracks or notches, plays a key role during the fracture initiation process. In many cases, notched elements are studied as cracked components for the sake of simplicity (e.g., Whittaker et al. 1992; Jaeger et al. 2007), but this approach may be over-conservative. A notch affects the rock strength or apparent fracture toughness depending on the notch radii. For large radii, almost no stress concentration occurs at the notch tip and, therefore, the notch would simply involve a section reduction rather than acting as a stress riser. For smaller radii, significant stress concentrations occur at the notch tip and the load-bearing capacity is reduced. For very small radii, i.e. “sharp” notches, the load-bearing capacity is no longer reduced because of the discontinuous nature of the material at the microscale. Thus, the notch effect depends on the material microstructure.

The study of the notch effect is crucial in many engineering rock fracture mechanics problems, since most of the defects that appear in rocks, no matter whether they are naturally created or man-made, have a finite radius and can be studied as notch-type defects. The authors have previously performed exhaustive laboratory campaigns on the notch effect in several rocks (Justo et al. 2017). The results of those laboratory campaigns show a dependence of the notch effect on the critical distance of the rocks. The critical distance is an intrinsic property of the material, and the larger it is the lower the observed notch effect. Likewise, the critical distance

somehow depends on the grain size of the material (Taylor 2017). Thus, the grain size seems to have an influence on the notch effect. However, many real rock features make detailed analyses difficult, such as inhomogeneities, grain size distribution, grain aspect ratio, porosity, etc. Consequently, numerical analyses provide a suitable alternative for investigating the influence of grain characteristics on the notch effect of U-shaped rock beams.

To interpret the notch effect, different fracture mechanical methodologies are available. Here, the Theory of Critical Distances (TCD) will be used because it is the same methodology as that used by the authors to interpret the notch effect from laboratory tests (Justo et al. 2017). The TCD is a stress-based local methodology widely used in the last few decades thanks to its potential and capabilities. A complete review of the TCD is given by Taylor (2007). It consists of a group of methodologies with some common features, as the use of a material characteristic parameter called the critical distance (L) and the use of linear elastic analyses when performing fracture assessments. The origins of the TCD can be dated back to the mid-twentieth century with the works of Neuber (1958) and Peterson (1959). However, this methodology did not grow until some time later with the development of finite element stress analyses, which allowed this theory to be scientifically analysed and successfully applied to different materials and failure conditions (e.g., Taylor & Wang 2000; Susmel & Taylor 2003; Susmel & Taylor 2010; Cicero et al. 2012; Cicero et al. 2014; Justo et al. 2017). Once the critical distance (L) is defined for a certain material, it is straightforward to assess the load-bearing capacity of any component made of this material. The real physical meaning of the critical distance (L) is still under research and discussion. However, it is generally related to the microstructural properties and to what is broadly referred to as the Fracture Process Zone (FPZ). This process zone is developed in rocks as a consequence of the initiation and coalescence of microcracks in front of the defect tip when increasing the applied load level. Parisio et al. (2019) studied the characteristics of the FPZ in granite both experimentally and using finite element analyses, and highlighted the importance of dissipative phenomena related to the microcracking and to the size of the FPZ when analysing brittle failure of rocks. This FPZ has been found to be related to the grain size (e.g., Brooks et al. 2012). Similarly, Taylor (2017) tried to relate L with a clearly identifiable microstructural distance (d) which, in the case of metals, ceramics and rocks, could be related to the grain size. The authors also related L with the mean grain size of different rocks using laboratory experiments (Justo et al. 2017); and here, this relationship is investigated using numerical analyses of ideal rocks.

Jenabidehkordi (2018) provides a review of the computational methods for fracture in rocks and classifies them into three categories: continuum based methods, discrete crack approaches and block-based methods. Continuous approaches and discrete crack methods might be suitable options when global responses are of interest (e.g., Yingren & Shangyi 2004), but they are less appropriate for applications where detailed information around a crack tip is required. By contrast, the block-based methods model the rock masses as an assembly of blocks with interfaces (or contacts) between them and allow simulations of large displacements, rock fracturing, taking into account the interaction of the fractured rock fragments.

One of the most popular block-based approaches is the Discrete Element Method (DEM), which was first proposed by Cundall (Cundall 1971; Cundall 1988). The DEM has been widely used to model fractures and fracturing in the field of rock mechanics, as for example in jointed rock masses (Huang et al. 2015; Scholtès & Donzé 2012), tunnelling (Kochen & Andrade 1997), borehole and well stability (Rawlings et al. 1993) or reservoir simulations (Gutierrez & Makurat 1997). The Universal Distinct Element Code (UDEC) refers to a particular DEM scheme that uses deformable contacts and an explicit, time-domain solution scheme. UDEC has been extensively

used by many authors for rock fracture numerical analyses. For example, based on Voronoi blocks, Chen & Konietzky (2014) developed and implemented a grain-based heterogeneous numerical model to simulate the time-dependent fracturing process of granite, analysing both intergranular and intragranular fracturing. Similarly, Nicksiar & Martin (2014) studied the factors affecting crack initiation based on a grain-based model, also using the Voronoi tessellation scheme to represent low porosity crystalline rocks such as granites. Wong et al. (1996), on the other hand, studied the effect of the initial microcrack density and grain size on the uniaxial compressive strength of different marbles. All these previous studies, among others, show the importance of the microstructure of rocks on their macroscopic behaviour and, in particular, the influence of the grain size on the fracture assessment of the rocks.

Several authors (e.g., Gui et al. 2016; Li et al. 2017; Wang et al. 2019) have studied the influence of the grain size on the fundamental rock properties. Gui et al. (2016) investigated the grain size effect simulating Brazilian disks and uniaxial compressive tests with different polygonal grain assemblages using distinct element analyses. They reported that larger particle size produces higher stiffness and strength of the intact rock. The ceramic literature has a mature history on the correlation of fracture toughness and grain size. However, some research data report results that are ambiguous: Gutshall & Gross (1969) indicated that fracture toughness increases with the grain size as a consequence of the preponderance of transgranular fracture shown in large grain materials. By contrast, Evans & Davidge (1969) showed a decrease of the fracture toughness with the increase of the grain size of a different polycrystalline material.

The problem of the size effect has proven to be of great importance in the branch of geotechnical engineering and Bazant (1999) provided a broad review on this issue. The development of increasingly realistic models that use a material characteristic length to define the size of the FPZ has led in the last decades to several works dedicated to size effects on the fracture behaviour of brittle materials. Tarokh & Fakhimi (2014) used a discrete element approach with a softening contact bond model to simulate the development of the FPZ in three-point bending tests of quasi-brittle materials, and reported that the width of the process zone is a linear function of particle radius. Similarly, Galouei & Fakhimi (2015) simulated three-point bending tests using a bonded particle model to study the effect of specimen size and material ductility on the shape of the FPZ of quasi-brittle materials. Tarokh et al. (2017) studied experimentally and numerically (using DEM with a tension softening contact bond model in this case) the development of the process zone with the specimen size in rocks and showed that both, length and width of the process zone increase with the increase of the specimen size. Liu et al. (2018) used an exponential softening contact bond model to address the size effects and the particle size issue.

With all this, taking as a basis the extensive literature on the use of DEM to study the influence of particle size on fundamental rock properties, this work aims to study the influence of the grain size on the fracture behaviour of U-shaped notched rock beams under mode I loading conditions. In particular, the focus is placed on the analysis of the notch effect through the variation of the apparent fracture toughness and the correlation between the grain size and the critical distance of the material, which is a key parameter for fracture assessments according to the TCD. Thus, the influence of the grain size on the notch effect is analysed. Additionally, the effect of the grain size on several macroscopic properties of the analysed rock is also investigated, such as Young's modulus, Poisson's ratio, tensile strength and fracture toughness. The influence of the grain size in these latter parameters has previously been analysed in the literature as mentioned above, but are included here to provide a more complete vision of the

studied case and to corroborate previously observed trends, which in some cases are still not fully clear (as for example the variation of the fracture toughness with the grain size depending on inter- or intragranular fractures). In this work, Voronoi block-based DEM is used to model crack initiation in low porosity crystalline rocks. An ideal rock material that resembles the Macael marble tested by the authors (Justo et al. 2017) has been studied and 5 different grain sizes are considered, namely 1, 1.5, 2, 2.5 and 3 mm. The modelled grains are relatively large (compared to those of the Macael marble) due to computational capacity limitations and present a highly uniform distribution. However, these considerations facilitate the analyses and the interpretation of the results.

In conclusion, the aim of this paper is to numerically study the notch effect in 5 ideal rocks (non-porous, crystalline, uniform and isotropic), with different grain sizes. The interpretation of the notch effect is performed using the TCD, specifically the Line Method (LM), which is briefly presented in Section 2. The analysis is based on DEM simulations. The numerical model, hypotheses and parameters are portrayed in Section 3. The results and their interpretation, both in general terms and using the LM, are presented in Section 4. Finally, some conclusions are provided.

2. INTERPRETATION OF NOTCH EFFECT THROUGH THE TCD

In this paper, the assessment of the fracture behaviour of the notched specimens is performed using the TCD, and more specifically the LM. This methodology considers a local failure criterion based on the stress field at the notch tip. Basically, the LM states that failure occurs when the average stress over a certain distance (d) starting at the notch tip is equal to the inherent strength (σ_0) of the rock:

$$\frac{1}{d} \int_0^d \sigma(r) dr = \sigma_0 \quad (1)$$

In the case of quasi-brittle materials such as rocks with nearly linear elastic behaviour, σ_0 can be assumed to roughly coincide with the tensile strength (σ_u), as claimed by Taylor (2007).

The LM of the TCD relates the distance d over which the stress is averaged with a parameter known as the critical distance (L). This parameter is characteristic of the analysed material and has length units in the order of a few millimetres in the case of rocks (Cicero et al. 2014; Justo et al. 2017). The expression for L is as follows:

$$L = \frac{1}{\pi} \left(\frac{K_{IC}}{\sigma_0} \right)^2 \quad (2)$$

It can be analytically demonstrated that $d = 2L$, based on the stress field at the crack tip at failure provided by Anderson (2004) as a function of distance from the tip (r) and the material fracture toughness (K_{IC}):

$$\sigma(r) = \frac{K_{IC}}{\sqrt{2\pi r}} \quad (3)$$

With this, the failure criterion defined by Equation 1 can be rewritten as:

$$\frac{1}{d} \int_0^d \frac{K_{IC}}{\sqrt{2\pi r}} dr = \frac{2 \cdot K_{IC}}{\sqrt{2\pi d}} = \sigma_0 \quad (4)$$

Isolating d from Equation 4 the following expression is obtained:

$$d = \frac{2}{\pi} \left(\frac{K_{IC}}{\sigma_0} \right)^2 \quad (5)$$

which is two times the critical distance defined by Equation 2. Thus, the failure criterion of the LM can be rewritten as:

$$\frac{1}{2L} \int_0^{2L} \sigma(r) dr = \sigma_0 \quad (6)$$

This research uses the LM for the fracture assessment of U-notched rock specimens. To this end, the fracture analysis is equated to a situation in a cracked component where the apparent fracture toughness (K_{IN}) is considered instead of the real fracture toughness (K_{IC}). K_{IC} corresponds to a cracked situation in which the notch radius (ρ) is theoretically equal to zero; thus, the notch effect is considered through K_{IN} .

An analytical expression for the calculation of K_{IN} may be obtained using the LM and the stress distribution at the notch tip. The stress distribution normal to the notch plane ($\sigma(r)$) has been studied by many authors in the past (e.g., Timoshenko & Goodier 1951; Weiss 1962; Creager & Paris 1967). For example, the stress along the bisector of the notch is given by Creager and Paris (1967) as:

$$\sigma(r) = \frac{K_I}{\sqrt{\pi}} \frac{2(r + \rho)}{(2r + \rho)^{3/2}} \quad (7)$$

where r is the distance from the tip, ρ is the notch radius and K_I is the stress intensity factor for a crack with the same length as the notch. Integrating Equation 7 in the domain defined by Equation 6 and considering that failure will occur when K_I is equal to K_{IN} , the following result is obtained:

$$\sigma_0 = \frac{2 \cdot K_{IN}}{\sqrt{\pi}} \cdot \frac{1}{\sqrt{\frac{\rho}{2} + 2L}} \quad (8)$$

By definition, K_{IN} is equal to K_{IC} when the notch radius is equal to zero. Thus, the previous expression can be rewritten for $\rho = 0$ as follows:

$$K_{IC} = \sigma_0 \sqrt{\frac{\pi}{2}} \cdot L \quad (9)$$

With all this, developing Equation 8 and considering the definition of K_{IC} in Equation 9, the following analytical solution is obtained for the LM of the TCD:

$$K_{IN} = K_{IC} \sqrt{\frac{\rho}{4L} + 1} \quad (10)$$

With this expression, the notch effect (i.e. the variation of K_{IN} with ρ) and the influence of the grain size on it will be analysed. In particular, the variation with the grain size of both L and K_{IC} , which are key parameters for the determination of the fracture initiation, is considered. To this end, several numerical analyses are performed.

This approach is strictly only valid within the framework of Linear Elastic Fracture Mechanics (LEFM), assuming a negligible plastic process zone. This hypothesis has already been validated by the authors in previous works for a group of rocks, where successful load fracture predictions

were performed using the same geometry and notches studied in this work and applying the TCD (Justo et al., 2017) and the Strain Energy Density criterion (Justo et al., 2018), both of them based on LEFM. This approach provided relatively accurate results even when analysing the rocks at high temperatures up to 250°C (Justo et al., 2020). The applicability of LEFM was discussed more in detail in this last work.

3. NUMERICAL MODELS

3.1. Methodology

Among the existing block-based approaches for the fracture analyses of rocks the DEM is used in this work. The DEM is a numerical technique to simulate the behaviour of a population of independent particles (Cundall and Strack, 1979). Each particle is represented numerically and is identified with its specific properties (e.g., shape, size, material properties, initial velocity). The DEM allows finite displacements and rotations of these discrete particles as a consequence of the interaction through their contacts, including complete detachment, and recognizes new contacts automatically as the calculation progresses. In this work, UDEC v6.00 (Itasca 2010) is used for the construction and analyses of the different numerical models.

The grains are represented by deformable blocks that are subdivided into finite-difference elements (zones), and each element responds according to a prescribed stress-strain law that will be defined in the following subsections. Likewise, the discontinuities stand for the boundaries (joints) between the grains (blocks), and their relative motion is governed by force-displacement relations for movement both in the normal and shear directions.

3.2. Model geometries

In order to represent the grains of the rocks in the numerical models, Voronoi tessellation is used to create randomly sized polygonal blocks. These Voronoi polygons are defined by an average edge length (l), which is varied in this work to analyse the effect of the grain size on the fracture of the rocks. On the other hand, the size homogeneity of the Voronoi polygons is defined by the number of iterations (n) in the relaxation process during the generation of the mesh. The more iterations, the more homogeneous the polygons will be in terms of size. In this work, the number of iterations (n) has been set to 30 in all the simulations, which has been considered as an appropriate value for a uniform distribution of the grain size. The considered values for l are 1, 1.5, 2, 2.5 and 3 mm, as depicted in Figure 1.

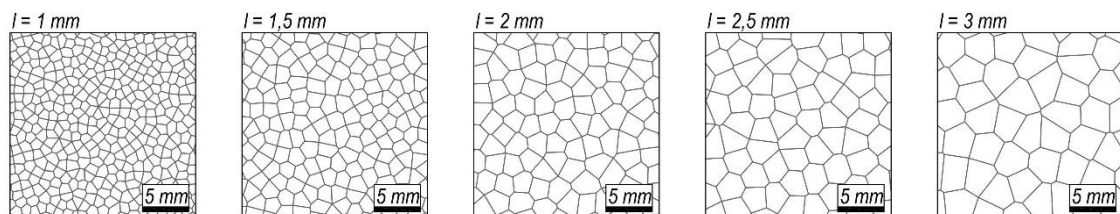


Fig. 1.- Representation of the Voronoi tessellations with different average edge length (l).

Figure 2 provides the size distribution curves of modelled grains. Both, frequency and cumulative frequency are represented in percentage. Grain diameter corresponds to the diameter of ideally circular grains with the same area as the actual modelled grains.

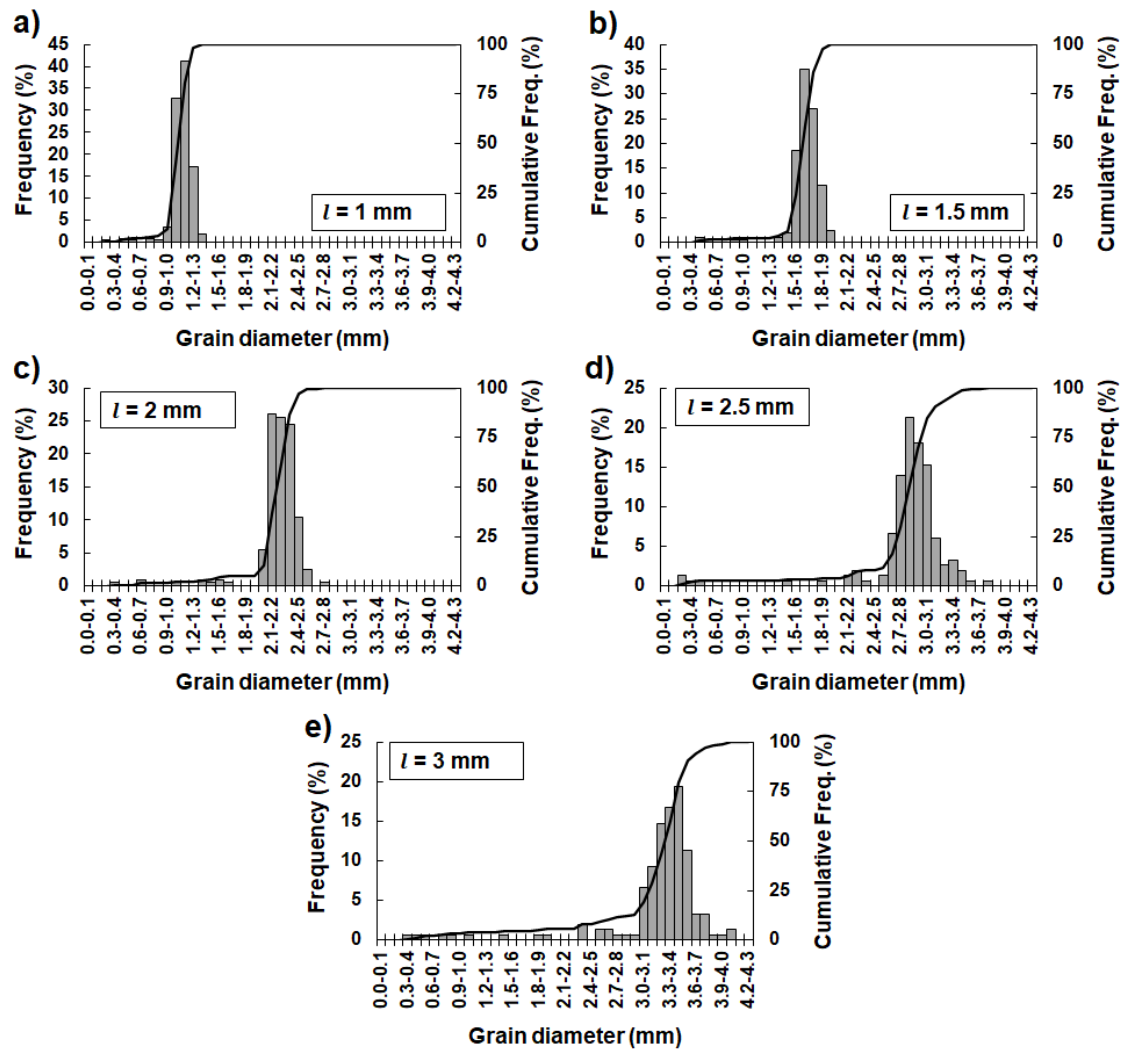


Fig. 2.- Size distribution curves of the modelled grains defined by an average length l of (a) 1 mm, (b) 1.5 mm, (c) 2 mm, (d) 2.5 mm and (e) 3 mm.

The observed outlier values below the average grain diameter correspond to grains located at the outer boundaries of the region defined by the Voronoi tessellation and, therefore, do not affect the crack propagation zone. Table 1 gathers some statistical values of the grains, namely the mean grain diameters, the standard deviations and the sorting coefficients defined as the ratio between the first and third quartiles (Q1 and Q3, respectively). This latter parameter indicates that the size distribution is relatively uniform as the coefficient is close to 1 in all the cases.

Table 1.- Statistical parameters of the modelled grain sizes.

	$l=1\text{mm}$	$l=1.5\text{mm}$	$l=2\text{mm}$	$l=2.5\text{mm}$	$l=3\text{mm}$
Mean grain diameter (mm)	1.109	1.659	2.213	2.829	3.187
Standard deviation (mm)	0.132	0.194	0.290	0.505	0.631
Sorting coef. (Q1/Q3)	1.110	1.092	1.083	1.096	1.095

The blocks are discretized into constant-strain finite-difference triangular zones, as shown in Figure 3. The zones are defined by the maximum edge length (e) of the triangles composing the mesh, which has been set to the same value as the average block edge length. In this way, the proportion of zones within the blocks remains roughly constant.

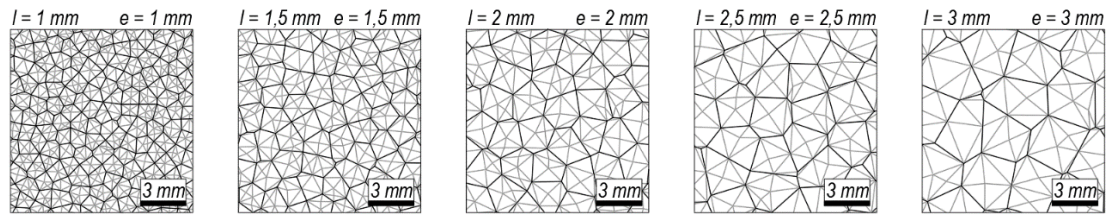


Fig. 3.- Representation of the zones within the Voronoi polygons.

Different numerical models have been constructed. These models consist of tensile splitting (Brazilian) tests (Figure 4a), simple compression tests (Figure 4b) and four-point bending tests (Figure 4c), all of them under plane strain conditions. Compression models are not strictly necessary for the performed fracture analyses, but they are also studied for a better characterisation of the simulated materials through the Young's modulus. In these models the crack initiation is not necessarily associated with failure (e.g., Nicksiar & Martin 2014), since scattered microcracks may arise before reaching the compression strength of the material. In any case, the obtained stress-strain curves are linear from the onset of loading and the estimated Young's modulus values correspond to the secant modulus at 50% of the peak strength (E_{50}). In the case of uniaxial compression, crack initiation and peak load are very different (e.g., Yue et al. 2017). This is due to the fact that, at low load level, a lot of microcracks start to develop in a diffuse manner, but later coalescence takes place and leads to a macroscopic crack and final failure. However, this is different when dominant tensile failure is analysed. Whenever a tensile crack of a certain size has been created, critical crack growth starts and failure follows immediately. Under these circumstances crack initiation and peak loads are very close. This statement is relative to the analysed scale, since when moving deeper into the microscale (e.g., μm , nm , etc.) the difference between crack initiation and peak load will increase. Here, considering the scale of the modelled grains (i.e., of the order of millimetres), the crack initiation load can be - in a first approximation - set equal to the tensile strength (σ_u) obtained from Brazilian test models (Figure 4a) and to analyse the notch effect from the four-point bending models (Figure 4c). Different authors (e.g., Dan & Konietzky 2014) have shown Brazilian test simulations where crack initiation and peak strength are very close to each other. Hoek & Martin (2014) assume that when dominant tensile failure occurs, as in the case of Brazilian and four-point bending tests, crack initiation and peak strength are very close.

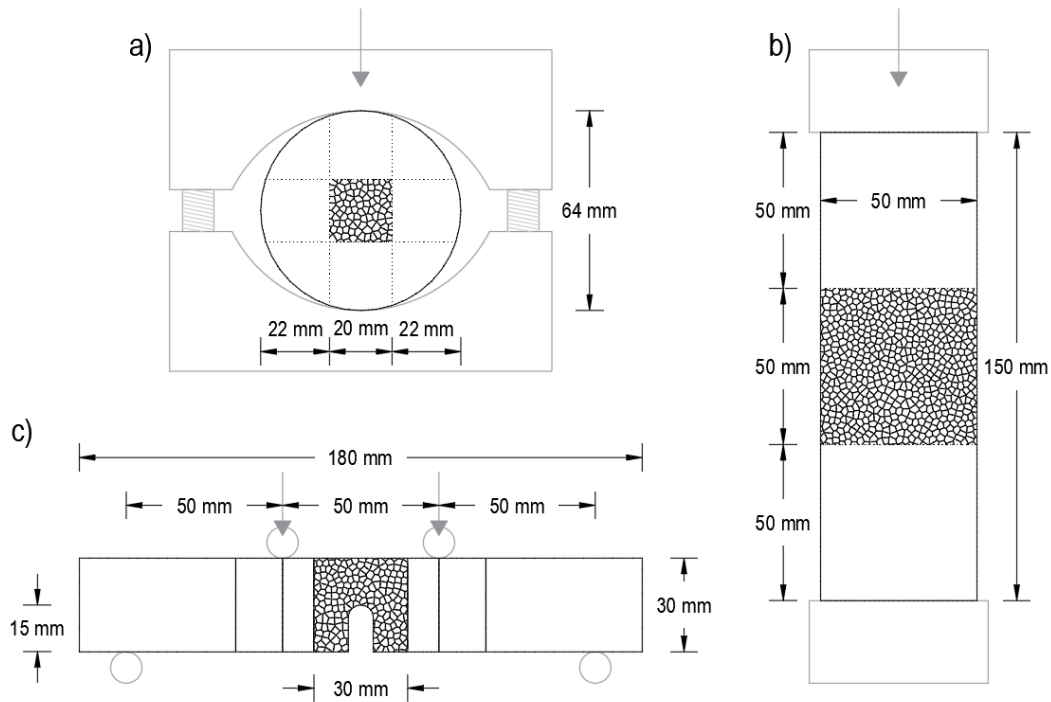


Fig. 4.- Representation of the simulated numerical models corresponding to tensile splitting (Brazilian) tests (a), simple compression tests (b) and four-point bending tests (c).

3.3. Material parameters

For the intact blocks, a linearly elastic isotropic behaviour has been assumed in this work, which only requires two parameters: the bulk modulus (K) and the shear modulus (G). This means that the grains are supposed to be homogeneous, isotropic and exhibit a linear stress-strain behaviour with no hysteresis on unloading. The rock is idealized as an assembly of unbreakable grains. Thus, cracks can only propagate along the boundaries.

The Coulomb slip model with residual strength is considered to model the interaction between grains. This model provides a linear representation of joint stiffness and yield limit, and is based upon elastic stiffness, frictional, cohesive and tensile strength properties, and dilation characteristics common to rock joints (Itasca 2010). Here, the term joint refers to the contact between grains. The residual strength simulates displacement-weakening of the joint by loss of frictional, cohesive and/or tensile strength at the onset of shear or tensile failure. That is, an internal fracture flag is set for each joint segment when the tensile or shear strength is exceeded. Thus, when a joint is fractured, the joint tensile strength, the joint friction angle and the joint cohesion are set to residual values.

In order to make the models more computationally efficient and less time-consuming, the Voronoi tessellation has only been generated in the vicinity of the notch (as shown in Figure 4) where the fracture is starting. The remaining parts of the model are also composed by deformable blocks with the same constitutive model as the intact blocks but different internal meshing. To ensure that no sliding or opening is occurring in the contact between these blocks and the region with Voronoi polygons, these contacts are defined as “joined” contacts with high values of the joint cohesion and tensile strength.

The calibration process of the required parameters is based on the experimental results obtained by the authors in previous works (Justo et al. 2017; Justo et al. 2018), particularly on the results of the Macael marble due to the low porosity, isotropic, uniform and relatively

homogeneous distribution of grain size, with a crystalline structure and no matrix around it. Table 2 gathers the mechanical properties of the Macael marble that were obtained in the laboratory. However, it is not the purpose of this research to simulate the exact behaviour of this marble because of its smaller grain size, but to model rock-like materials with comparable properties and within a realistic order of magnitude. Indeed, the main objective of this work is to analyse the effect of the grain size of a geomaterial like a rock on the crack initiation. In order to obtain conclusions as clear as possible and to avoid the influence of other possible factors other than grain size, the performed analyses have been simplified by modelling ideal rock materials with non-porous crystalline structure (only grains, without matrix), similar to the metamorphic marbles analysed by the authors (Justo et al. 2017). In addition, relatively large grain sizes with mean edge lengths from 1 to 3 mm have been studied due to computational capacity reasons.

Table 2.- Mechanical properties of the Macael marble.

Parameter	Value
Bulk density (kg/m ³)	2715
Young's modulus, E_{50} (GPa)	73.4
Poisson's ratio, ν	0.28
Tensile strength, σ_u (MPa)	9.97
Fracture toughness, K_{IC} (MPa·m ^{1/2})	1.14

All the parameters in Table 2 correspond to the rock behaviour at the macro-scale. The properties of the individual grains do not have to be strictly the same, but in this case, considering the homogeneity of the studied rock, the values in Table 2 have been taken as the basis for the calculation of the bulk (K) and shear (G) modulus of the grains:

$$K = \frac{E}{3(1 - 2\nu)} \quad (11)$$

$$G = \frac{E}{2(1 + \nu)} \quad (12)$$

Table 3 gathers the parameters of the material constitutive model used for the definition of the linearly elastic isotropic behaviour of the rock grains, derived from the values in Table 2.

Table 3.- Parameters for the linearly elastic isotropic constitutive model of the grains.

Parameter	Value
Bulk density (Kg/m ³)	2715
Bulk modulus, K (GPa)	56
Shear modulus, G (GPa)	29

These parameters define the behaviour of the grains. However, their contact conditions have to be adjusted in order to obtain the desired behaviour at macro-scale. As a result of the calibration process, the parameters of the considered joint constitutive model, namely the Coulomb slip model with residual strength, are summarised both in Table 4 and 5. The former includes the joint cohesion, dilatation, friction and tensile properties and their residual values, while the latter gathers the zone size dependent parameters, that is, the normal and shear stiffness of the joints.

Table 4.- Parameters for the Coulomb slip constitutive model with residual strength.

Parameter	Value
Joint cohesion, j_c (MPa)	24.5
Joint dilatation angle, j_d ($^\circ$)	5
Joint friction angle, j_f ($^\circ$)	35
Joint tensile strength, j_t (MPa)	49.0
Joint residual cohesion, j_{resc} (MPa)	0
Joint residual friction angle, j_{rf} ($^\circ$)	25
Joint residual tensile strength, j_{rt} (MPa)	0

Table 5.- Zone size dependent stiffnesses for the Coulomb slip constitutive model with residual strength.

Parameter	Value
Joint normal stiffness, j_{kn} (GPa/mm) - $l = 1$ mm	1880
Joint shear stiffness, j_{ks} (GPa/mm) - $l = 1$ mm	938
Joint normal stiffness, j_{kn} (GPa/mm) - $l = 1.5$ mm	1250
Joint shear stiffness, j_{ks} (GPa/mm) - $l = 1.5$ mm	626
Joint normal stiffness, j_{kn} (GPa/mm) - $l = 2$ mm	938
Joint shear stiffness, j_{ks} (GPa/mm) - $l = 2$ mm	469
Joint normal stiffness, j_{kn} (GPa/mm) - $l = 2.5$ mm	751
Joint shear stiffness, j_{ks} (GPa/mm) - $l = 2.5$ mm	375
Joint normal stiffness, j_{kn} (GPa/mm) - $l = 3$ mm	626
Joint shear stiffness, j_{ks} (GPa/mm) - $l = 3$ mm	313

Very high values for the joint stiffnesses lead to a slow response and a slow solution convergence of the models without a significant change in the behaviour of the system, as the timestep calculation is based upon stiffnesses. For this reason, both the joint normal stiffness (j_{kn}) and the shear stiffness (j_{ks}) should be kept smaller than a factor times (usually 10) the equivalent stiffness of the stiffest neighbouring zone in blocks adjoining the joint (Itasca 2010):

$$j_{kn} \& j_{ks} \leq 10 \left[\max \left[\frac{K + \frac{4}{3}G}{\Delta z_{min}} \right] \right] \quad (13)$$

where K and G are those of the block material, and Δz_{min} is the smallest width of the zone adjacent to the joint in the normal direction. As a general criterion in the performed simulations, Δz_{min} has been set to half of the maximum edge length established for the zones. There may also be problems with block interpenetration if the normal stiffness is very low, as the contact overlap between blocks can be excessively large. On this basis, the normal stiffness (j_{kn}) has been set to the limit value defined by Equation 13.

Furthermore, the ratio of the normal to shear stiffness (j_{kn}/j_{ks}) dramatically affects the Poisson response of a rock mass (Itasca 2010). When the shear stiffness is equal to the normal stiffness ($j_{kn} = j_{ks}$) the Poisson effect is zero. Thus, for a more realistic representation of the Poisson effect, the ratio j_{kn}/j_{ks} must be larger than unity. Several articles can be found in the literature dealing with this topic (e.g., Asadi & Barla 2012; Nassir et al. 2013). Here, $j_{kn}/j_{ks} = 2$ has been adopted, which is assumed to be a reasonable ratio (see Table 5).

Anticipating to the results obtained in Section 4, the parameters used in the numerical models (Tables 3, 4 and 5) lead to a relatively similar macro-scale response as that obtained

experimentally for the Macael marble (Justo et al., 2018) in terms of tensile strength and deformational parameters such as the Young's modulus and the Poisson's ratio (Table 2 represents the macroscopic parameters of the Macael marble). In general, the numerically obtained macroscopic parameters are slightly higher (around 20% in the case of the tensile strength and the Poisson's ratio). The obtained macroscopic properties are summarised in Section 4.

3.4. Boundary conditions

With regards to the model boundary conditions, a constant loading velocity has been applied in all the cases (Figure 4) to simulate the real laboratory test conditions that are performed under displacement control. The applied velocity is sufficiently small to ensure quasi-static responses of the numerical models.

The user-specified velocity is input to the model as an exterior boundary condition and viscous damping is specified for the blocks to avoid dynamic effects. The specified damping conditions cause the vibrational energy to be absorbed in proportion to the rate of change of the kinetic energy. Here, the ratio of damping dissipation to kinetic energy change has been set equal to 0.5, which gives a relatively fast convergence and ensures that no dynamic effects will affect the results.

3.5. Repetitiveness

Using a discrete numerical model, the results will depend on the specific distribution of the Voronoi blocks representing the grains. For this reason, the meshes have been randomly generated and a minimum repetitiveness of 6 Voronoi tessellations have been used for each case. Besides, the symmetry with respect to the bisector plane of the notches (Figure 4) has not been considered when constructing the four-point bending test models because the distribution of the Voronoi blocks (grains) is not symmetric, as in reality.

The actual arrangement of the Voronoi polygons (or grains) produces a scatter of the results even when keeping the average grain size constant. For the particular case of the Brazilian tests and the four-point bending tests, the results show a visible scatter (mesh dependency) because the orientation of the grain contacts at the zone where the fracture starts notably influences the results.

4. RESULTS AND DISCUSSION

First, the results corresponding to the influence of the grain size on the elastic macroscopic properties (i.e., Young's modulus and Poisson's ratio) are presented. These results have no specific relation to the subsequent discussion of the fracture behaviour of the notched specimens but do provide important information on the characterization of the analysed rock. The obtained elastic macroscopic properties are compared to those obtained in a previous experimental campaign (Justo et al. 2017) for Macael marble. The objective of these first results is to define and delimit the characteristics of the rock-like material being analysed, in order to know to which real cases (equivalent to the model) the results could be related. Subsequently, the influence of the grain size on the fracture properties (i.e., tensile strength, apparent fracture toughness and fracture toughness) is analysed in more detail. In this case, in addition to comparing these properties with those of the Macael marble, their study is of special interest for the analysis of the notch effect through the TCD, which is the main objective of this work. According to the definition of the critical distance provided by Equation 2, the grain size

dependence of both, tensile strength (σ_u) and fracture toughness (K_{IC}), will define the variation of L with the grain size. Besides, the failure criterion defined by the LM of the TCD (Equation 6) limits the average stress over a distance $2L$ from the notch tip to σ_u . Thus, the interpretation of the notch effect that, based on the TCD, arises from this failure criterion, is influenced by the proper characterization of these properties and, consequently, by the grain size.

4.1. Influence of grain size on elastic properties

Firstly, 6 compression test models were carried out for each of the considered grain sizes (Figure 4b), only varying the distribution of the grains. The performed models correspond to plane strain conditions. Thus, the obtained moduli stand for the plane strain situation ($E_{50,PSM}$), different from those obtained in the laboratory for cylindrical specimens (E_{50}). Both moduli are related through the Poisson's ratio (ν) with the following expression:

$$E_{50,PSM} = \frac{E_{50}}{1-\nu^2} \quad (14)$$

As a result, Figure 5 gathers 3 different curves. The plane strain modulus ($E_{50,PSM}$) and the Poisson's ratio (ν) are obtained directly from the compression test models for each of the grain sizes, considering the deformations within a 25x25mm square in the middle of the specimens. The obtained results are slightly sensitive to the size of this area (Ghazvinian et al. 2014). The numerically obtained $E_{50,PSM}$ values are corrected with Equation 14 to get E_{50} . The latter values of E_{50} are comparable to those obtained in the laboratory and correspond, as mentioned above, to the secant Young's modulus at 50% of the peak strength. The open symbols represent the individual values and the full symbols and solid lines represent mean values of the Young's moduli ($E_{50,PSM}$ & E_{50}) and Poisson's ratio (ν). Comparing the emergent macroscopic values of E_{50} and ν with those of the Macael marble (Table 2), slightly lower values of the Young's modulus and higher values of the Poisson's ratio are obtained.

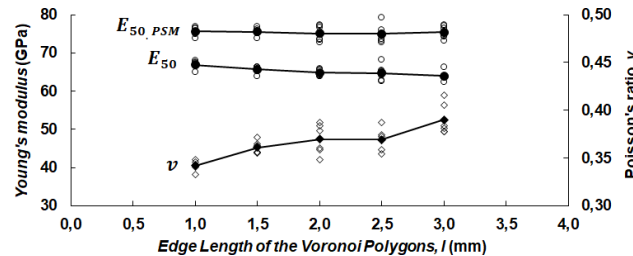


Fig. 5.- Variation of the Young's modulus ($E_{50,PSM}$ & E_{50}) and Poisson's ratio (ν) with the grain size.

According to Figure 5, in general terms, an increasing tendency with the grain size is observed in the case of the Poisson's ratio, which depends on the $jk\eta/jk\sigma$ relation (Ghazvinian et al. 2014). Gui et al. (2016) reported a similar increase in the Poisson's ratio with the grain size. By contrast, $E_{50,PSM}$ seems roughly constant with the grain size, which might be attributed to the variation of $jk\eta$ for each of the grain sizes in accordance with Equation 13. Gui et al. (2016), for example, reported an increase of the Young's modulus with the grain size but they kept $jk\eta$ constant in their simulations.

4.2. Influence of grain size on tensile strength

12 Brazilian test models have been run in this case for each of the analysed grain sizes. As an example, Figure 6 shows the obtained horizontal stresses (σ_{xx}) in a Brazilian test model at

the onset of cracking, from which the tensile strength of the material (σ_u) has been derived as mentioned above, and a picture of the generation of the first cracks.

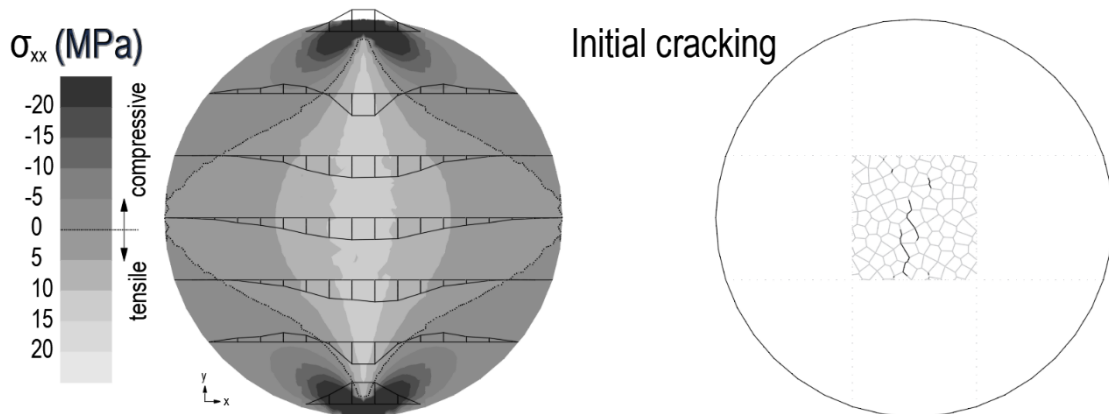


Fig. 6.- Example ($l = 2 \text{ mm}$) of the horizontal stresses of a Brazilian test model at the onset of cracking ($F = 11.37 \text{ kN/mm}$) and generated cracks once the strength is exceeded. Tensile stresses are positive.

The variation of the tensile strength with grain size is represented in Figure 7. A continuous increment of tensile strength is observed, which is in accordance with the results obtained by other authors. More specifically, a proportional variation of σ_u with the square root of the edge length (l) is observed, which has been adjusted by a linear law (grey solid line) that roughly coincides with the average values (black dashed line). Gui et al. (2016), for example, simulated six different Brazilian tests with Voronoi tessellation grains ranging from 1 to 6 mm and concluded that the tensile strength increases with the grain size used in the models. They stated that this could be caused by the fact that with an increase in the grain size, less potential fractures are included in the numerical models and, therefore, the characteristics of the models will be closer to intact rock.

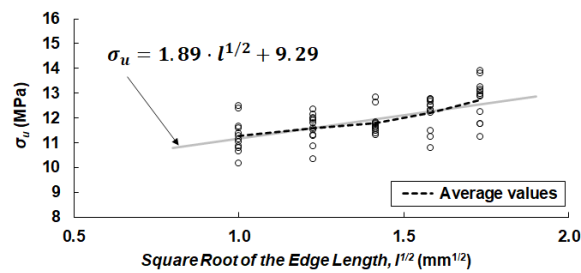


Fig. 7.- Variation of the tensile strength σ_u with the grain size.

4.3. Influence of grain size on notch effect

300 four-point bending tests have been modelled in total with a repetitiveness of 6 models per notch radius and grain size combination, only varying the randomly generated Voronoi mesh. In order to consider the notch effect, several notch radii have been incorporated in the four-point bending models, with radii (ρ) ranging from 1 mm to 15 mm. In this analysis, only intergranular failure is being considered. Thus, the cracks can only propagate along the boundaries of the grains. Consequently, the minimum radius of the aforementioned notches has been limited to the grain size in each case ($\rho \geq l$). This restriction intends to avoid the possibility of a notch not having at least one grain boundary at the tip, which could cause the breakdown of the calculation model due to the intergranular failure assumption.

For each of the individual numerical models of the four-point bending tests, the crack initiation load (F) has been calculated at the onset of failure, just at the moment prior to the appearance of the first crack. As shown in Figure 8, the bending moment between the loading points is constant in a four-point bending configuration ($M = F \cdot L/6$). At the same time, the horizontal stress (σ_{xx}) at the bisector of the notch can be equated to a bending moment (M) defined by a pair of forces (P) with a lever arm (z), where $M = P \cdot z$. Thus, the crack initiation load F (with force/depth length units) can be obtained comparing both expressions:

$$F = \frac{6 \cdot P \cdot z}{L} \quad (15)$$

where L is defined in Figure 4c (150 mm) and P and z are derived from the stress field obtained along the bisector of the notch just in the calculation step prior to development of the first crack.

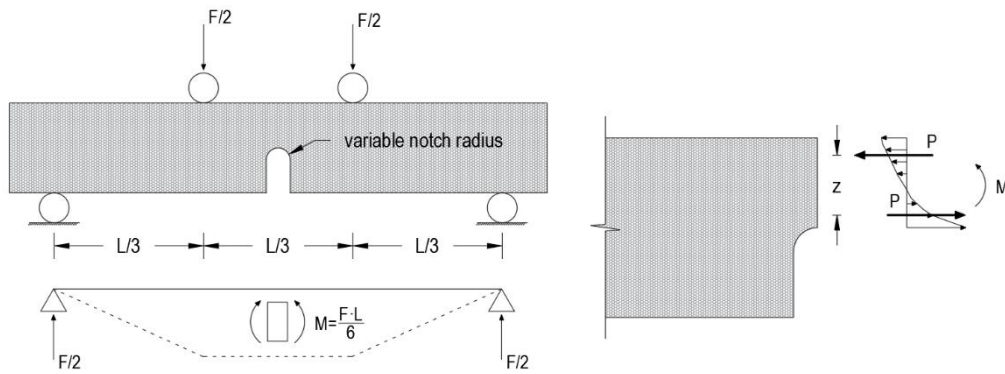


Fig. 8.- Scheme to illustrate bending moment in rock beam and stress field in the bisector of the notch.

Once the crack initiation load (F) is obtained, K_{IN} may be determined using the formulation proposed by Sawley & Gross (1976) for Single Edge Notched Bend (SENB) specimens as those simulated in this work (Figure 4c):

$$K_{IN} = \frac{F \cdot Y}{h^{1/2}} \quad (16)$$

where h is the specimen height, while Y stands for a compliance factor given by the following expression:

$$Y = \frac{3 \cdot (L_o - L_i) \cdot \alpha_0^{1/2} \cdot X}{2h \cdot (1 - \alpha_0)^{3/2}} \quad (17)$$

with

$$X = 1.9887 - \left[\frac{(3.49 - 0.68\alpha_0 - 1.35\alpha_0^2) \cdot \alpha_0 \cdot (1 - \alpha_0)}{(1 + \alpha_0)^2} \right] - 1.32\alpha_0 \quad (18)$$

L_o and L_i represent the spans between the outer supporting rollers and the inner loading points, respectively, and α_0 is the relative crack length defined as the ratio between the initial notch length (15 mm) and the total height (30 mm) of the specimen ($\alpha_0 = 0.5$) (Figure 4c). Figure 9 represents the stresses in the surrounding of the notch at the onset of cracking, from which the crack initiation load (F) is derived in each case.

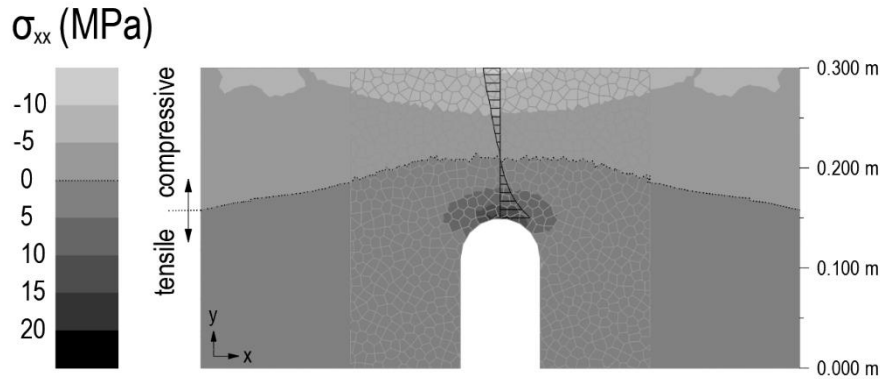


Fig. 9.- Example ($l = 1 \text{ mm}$; $\rho = 4 \text{ mm}$) of the horizontal stresses, σ_{xx} , of the four-point bending test models at the onset of cracking. Tensile stresses are positive.

With all this, Appendix A gathers the individual K_{IN} results of the four-point bending test models for each notch radii (ρ) and Voronoi edge lengths (l) that define the grain sizes (Figure 1).

To portray the notch effect, the results of the four-point bending models are graphically depicted in Figure 10. The individual results of the apparent fracture toughness summarised in Appendix A are represented by dots in Figure 10. K_{IN} increases gradually with the notch radius, so the notch effect is clear. The solid lines of the plots represent the best-fit curves according to Equation 10, leaving K_{IC} and L as free variables for the adjustment. By contrast, the dashed lines stand for the calculated curves, based once again on Equation 10 but using K_{IC} from the best-fit solution and L from Equation 2. A good agreement between both curves is observed in general terms. However, in the case of $l = 3 \text{ mm}$ the adjustment between the two curves is slightly worse (Figure 10e), which could be caused by the relatively large grain size with respect to the specimen geometry.

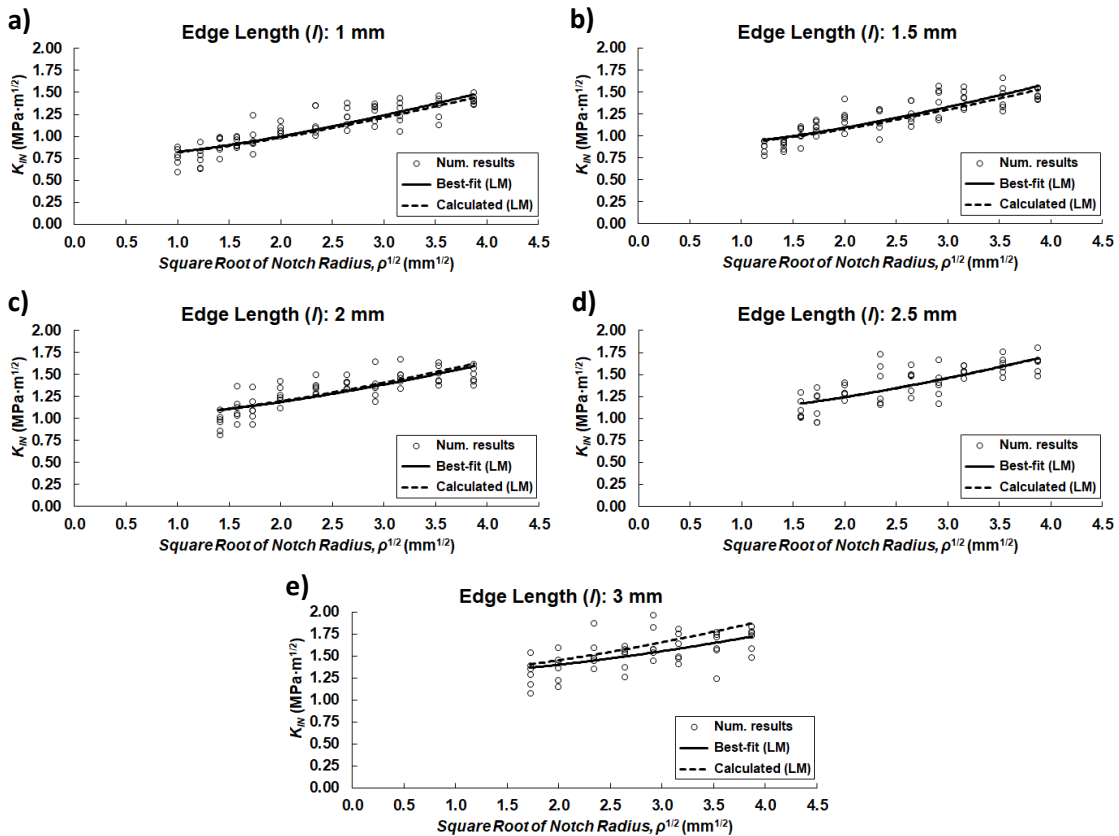


Fig. 10.- Variation of the apparent fracture toughness K_{IN} with the notch radius for each Voronoi edge length (l).

Figure 11 summarises in a single plot the best-fit curves represented in Figure 10. It is observed that, in general terms, the curves flatten and move upwards as the grain size increases. This means, respectively, a decrease in the notch effect and an increase in the fracture toughness with the grain size.

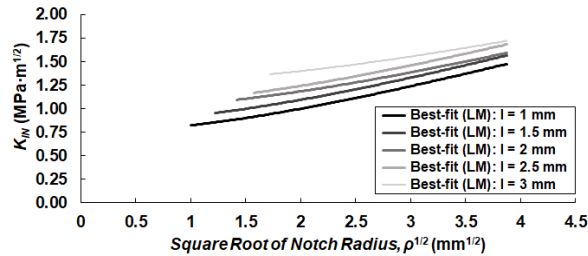


Fig. 11.- Summary of the best-fit curves of Figure 9.

4.4. Influence of grain size on fracture toughness

As mentioned above, the observed translation of the curves in Figure 11 indicate an increment of the fracture toughness of the rock specimens with the grain size. This effect was first discussed by Potyondy & Cundall (2004) and by many other authors since then (e.g., Moosavi et al. 2018). The fracture toughness reflects the residual strength of a component to crack propagation, or in other words, the fracture energy consumption rate required to generate new surfaces. Considering the intergranular failure assumption, the larger the grains the less potential grain boundaries for crack propagation and, therefore, K_{IC} will increase because higher fracture energy is required to generate new cracking surfaces. Figure 12 represents the variation of the fracture toughness with the grain size. The represented values are obtained from the best-fit curve adjustment of Equation 10 for each grain size.

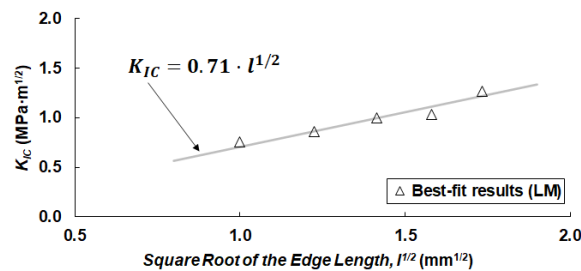


Fig. 12.- Variation of the fracture toughness K_{IC} with the grain size.

It is clearly observed that K_{IC} depends on the size of the grains. This is not surprising, as the concept of fracture toughness implies an internal length scale, whereby the ratio of fracture toughness to material strength has the dimensions of square root of length (Potyondy & Cundall 2004). In fact, Figure 12 shows that K_{IC} is proportional to the square root of the edge length (l) of the grain, which has also been suggested in previous studies (e.g., Duriez et al. 2016; Moosavi et al. 2018). Comparing these results with those depicted in Figure 7, the proportional increase of K_{IC} with l is notably larger than that of σ_u . Thus, according to Equation 2 that defines the critical distance as a function of the ratio K_{IC}/σ_u , certain dependency of L on the grain size is expected.

4.5. Influence of grain size on critical distance

Proceeding in a similar way, the critical distance can also be derived from the adjustment of the best-fit curves according to Equation 10 of the LM. These best-fit results are compared in Figure 13 to those calculated from Equation 2. The latter are calculated using the mean tensile strength obtained from the numerical models (Figure 7) and the fracture toughness from the best-fit curves (Figure 12). A good agreement is observed between the best-fit and the calculated results of L in all the cases except for the largest grain size. However, the consequences of this difference when performing failure load predictions are rather limited as shown by the authors (Justo et al. 2017; Justo et al. 2020), since L is squared in Equation 10.

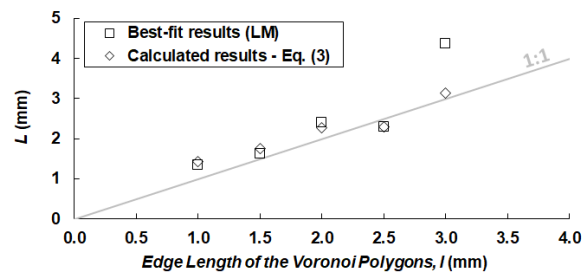


Fig. 13.- Variation of the critical distance L with the grain size.

All in all, a 1:1 linear relation is observed between the critical distance L and the grain size, L being of the order of the average edge length of the Voronoi polygons ($L \approx l$). This linear relation makes sense according to the definition of L provided by Equation 2 and considering the dependency of both K_{IC} and σ_u to grain size. As mentioned above, plane strain conditions are being considered, therefore, 3D effects are neglected here. Taylor (2017) analysed the relation of the critical distance (L) with clearly identifiable microstructural distances (d) such as the grain size of different materials, and concluded that in most of the cases, L is found to lie between d and $10d$. Thus, the obtained results in this work are located towards the bottom of the scatter band defined by Taylor (2017).

Finally, Table 6 summarises the parameters derived from the performed numerical analyses for each of the considered grain sizes, including the mean tensile strength, the fracture toughness and the critical distance from the best-fit and from the calculated case, all of them being key parameters for the fracture assessment according to the TCD.

Table 6.- Summary of the emergent macroscopic properties derived from the numerical analyses of each grain size.

	$l=1\text{mm}$	$l=1.5\text{mm}$	$l=2\text{mm}$	$l=2.5\text{mm}$	$l=3\text{mm}$
Young's modulus, E_{50} (GPa)	66.8	65.7	64.8	64.8	64.0
Poisson's ratio, ν	0.34	0.36	0.37	0.37	0.39
Tensile strength, σ_u (MPa)	11.29	11.59	11.79	12.20	12.74
Fracture toughness, K_{IC} (MPa \cdot m ^{1/2})	0.76	0.86	1.00	1.04	1.26
Critical distance, L (mm) – Best-fit	1.33	1.63	2.41	2.29	4.37
Critical distance, L (mm) – Calculated	1.43	1.76	2.27	2.30	3.13

5. CONCLUSIONS

DEM simulations have been performed to evaluate the influence of the grain size on the apparent fracture toughness of SENB specimens with U-shaped notches and with radii ranging from 1 up to 15 mm. As expected from the LFM theory and from experimental results (Justo et al. 2017), the simulated apparent fracture toughness increases with the notch radius, which reveals the notch effect. A comprehensive understanding of this effect is of special interest to perform accurate rock fracture assessments, since most defects in rock masses have finite radii and should be studied like notch-type defects rather than over-conservative crack-type defects. The TCD has proven to be an appropriate tool for the fracture assessment of notched rocks, considering the notch effect through the apparent fracture toughness. The observed variation of the apparent fracture toughness with the notch radii slightly decreases when the rock grain size increases, which seems to indicate that the notch effect softens with the increase of the grain size. This variation also implies an increase of the critical distance with the grain size, which can be derived both from the best-fit adjustment of the apparent fracture toughness results and from the analytical calculation of L using the numerically obtained values of the tensile strength and the fracture toughness.

The interpretation of the four-point bending tests using the TCD provided satisfactory results and values of the critical distance that corresponded to the grain size in a nearly 1:1 linear proportion. This correlation between the critical distance and the grain size must be understood only in qualitative terms because the numerical simulations are simply an idealization of the real problem (2D grains, only intergranular fractures) of an already highly idealised rock (non-porous, isotropic, very uniform grains with 1:1 aspect ratio) and due to the formulation of the model that is local.

To allow for an interpretation of the notch effect with the TCD, splitting (Brazilian) tests were also numerically simulated to obtain the tensile strength. It is observed that the tensile strength increases with the grain size but, proportionally, less than the fracture toughness. Additionally, simple compression tests were numerically simulated and an increase in the Young's moduli and Poisson's ratio with the grain size was found.

To conclude, this paper has shown the clear influence of the grain size on the notch effect in rocks and has gone deeper into the study of the physical meaning of the critical distance, which is a key parameter in the fracture assessment according to the TCD.

ACKNOWLEDGEMENT

The authors of this work would like to express their gratitude to the Spanish Ministry of Economy and Competitiveness for financing the National Plan Project (Ref.: BIA2015-67479-R) under the name of "The Critical Distance in Rock Fracture", and to the German Academic Exchange Service (DAAD) for the short-term research grant given to J. Justo for his research visit at TU Bergakademie Freiberg.

APPENDIX A

Table 7 gathers the individual apparent fracture toughness results obtained from the four-point bending test numerical models for each notch radii and grain size.

Table 7.- Summary of the results of the apparent fracture toughness.

ρ (mm)	$l = 1$ mm K_{IN} (MPa·m ^{1/2})	$l = 1.5$ mm K_{IN} (MPa·m ^{1/2})	$l = 2$ mm K_{IN} (MPa·m ^{1/2})	$l = 2.5$ mm K_{IN} (MPa·m ^{1/2})	$l = 3$ mm K_{IN} (MPa·m ^{1/2})
1	0,85				
1	0,79				
1	0,59				
1	0,76				
1	0,88				
1	0,70				
1,5	0,93	0,88			
1,5	0,72	0,77			
1,5	0,78	0,81			
1,5	0,63	0,94			
1,5	0,62	0,94			
1,5	0,83	0,88			
2	0,87	0,92	0,99		
2	0,97	0,96	0,86		
2	0,85	0,93	1,01		
2	0,97	0,89	0,96		
2	0,99	0,81	1,09		
2	0,74	0,84	0,81		
2,5	0,87	1,08	1,16	1,03	
2,5	0,96	1,07	1,03	1,09	
2,5	0,99	1,01	0,93	1,00	
2,5	0,89	1,10	1,04	1,19	
2,5	0,99	0,99	1,12	1,02	
2,5	0,89	0,85	1,37	1,30	
3	0,92	1,06	1,02	1,05	1,54
3	0,79	0,99	0,93	0,95	1,07
3	1,23	1,09	1,35	0,95	1,35
3	0,91	1,16	1,08	1,26	1,28
3	0,94	1,18	1,19	1,24	1,17
3	1,01	1,10	1,09	1,35	1,38
4	1,04	1,42	1,23	1,29	1,22
4	1,18	1,22	1,26	1,28	1,59
4	1,04	1,02	1,21	1,20	1,14
4	1,10	1,15	1,42	1,40	1,36
4	1,00	1,23	1,12	1,28	1,41
4	1,06	1,20	1,34	1,37	1,45
5,5	1,10	1,14	1,34	1,22	1,47
5,5	1,35	1,29	1,37	1,48	1,59
5,5	1,01	1,27	1,27	1,59	1,44
5,5	1,35	0,95	1,35	1,15	1,47
5,5	1,09	1,29	1,28	1,18	1,35
5,5	1,04	1,09	1,49	1,73	1,87
7	1,22	1,10	1,41	1,49	1,55
7	1,32	1,19	1,49	1,48	1,37
7	1,22	1,40	1,33	1,49	1,61
7	1,06	1,40	1,41	1,60	1,57
7	1,13	1,16	1,40	1,23	1,53
7	1,37	1,25	1,33	1,31	1,26
8,5	1,34	1,57	1,39	1,17	1,82
8,5	1,11	1,49	1,18	1,46	1,45
8,5	1,17	1,18	1,64	1,66	1,57
8,5	1,37	1,51	1,26	1,40	1,57
8,5	1,29	1,21	1,34	1,37	1,54
8,5	1,33	1,38	1,36	1,27	1,96
10	1,06	1,56	1,45	1,60	1,49
10	1,37	1,44	1,50	1,54	1,47
10	1,22	1,43	1,67	1,59	1,63
10	1,19	1,31	1,49	1,52	1,80
10	1,43	1,50	1,33	1,52	1,75
10	1,32	1,30	1,42	1,45	1,40
12,5	1,22	1,32	1,51	1,58	1,24
12,5	1,46	1,36	1,42	1,46	1,71
12,5	1,42	1,66	1,63	1,66	1,74
12,5	1,37	1,54	1,60	1,52	1,58
12,5	1,12	1,48	1,37	1,76	1,76
12,5	1,35	1,27	1,42	1,62	1,56
15	1,40	1,54	1,61	1,54	1,48
15	1,44	1,46	1,44	1,65	1,76
15	1,37	1,54	1,42	1,66	1,58
15	1,49	1,44	1,57	1,48	1,83
15	1,36	1,41	1,50	1,65	1,73
15	1,40	1,42	1,37	1,80	1,78

REFERENCES

- Anderson TL (2004) Fracture mechanics: fundamentals and applications, Third ed. CRC Press, Florida.
- Asadi MS, Barla G (2012) A bonded particle model simulation of shear strength and asperity segregation for rough rock fractures. *Rock Mech Rock Eng* 45:649-675.
- Bazant ZP (1999) Size effect on structural strength: a review. *Arch Appl Mech* 69:703-725.
- Brooks Z, Ulm FJ, Einstein HH (2012) Role of microstructure size in fracture process zone development of marble. 46th US Rock Mech/Geomech Symp 3:1748-1757.
- Chen W, Konietzky H (2014) Simulation of heterogeneity, creep, damage and lifetime for loaded brittle rocks. *Tectonophysics* 633(1):164-175.
- Cicero S, García T, Castro J, Madrazo V, Andrés D (2014) Analysis of notch effect on the fracture behaviour of granite and limestone: an approach from the theory of critical distances. *Eng Geol* 177:1-9.
- Cicero S, Madrazo V, Carrascal IA (2012) Analysis of notch effect in PMMA by using the Theory of Critical Distances. *Eng Fract Mech* 86:56–72.
- Creager M, Paris C (1967) Elastic field equations for blunt cracks with reference to stress corrosion cracking. *Int J Fract* 3:247–252.
- Cundall PA (1971) A computer model for simulating progressive large scale movements in blocky rock systems. *Proc Symp Rock Fracture (ISRM)* 1.
- Cundall PA (1988) Formulation of a three-dimensional distinct element model part I. A scheme to detect and represent contacts in a system composed of many polyhedral blocks. *Int J Rock Mech Min Sci* 25:107-116.
- Cundall PA, Strack ODL (1979) A Discrete Numerical Model for granular assemblies. *Geotechnique* 29:47-65.
- Dan DQ, Konietzky H (2014) Numerical simulations and interpretations of Brazilian tensile tests on transversely isotropic rocks. *Int J Rock Mech Min Sci* 71:53-63.
- Duriez J, Scholtès L, Donzé FV (2016) Micromechanics of wing crack propagation for different flaw properties. *Eng Fract Mech* 153:378-398.
- Evans AG, Davidge RW (1969) The strength and fracture of stoichiometric polycrystalline UO₂. *J Nucl Mat* 33(3):249-260.
- Galouei M, Fakhimi A (2015) Size effect, material ductility and shape of fracture process zone in quasi-brittle materials. *Comput Geomech* 65:126-135.
- Ghazvinian E, Diederichs MS, Quey R (2014) 3D random Voronoi grain-based models for simulation of brittle rock damage and fabric-guided micro-fracturing. *J Rock Mech Geotech Eng* 6:506-521.
- Gui YL, Zhao ZY, Ji J, Wang XM, Zhou KP, Ma SQ (2016) The grain effect of intact rock modelling using discrete element method with Voronoi grains. *Geotech Lett* 6:1-8.
- Gutierrez M, Makurat A (1997) Coupled htm modelling of cold water injection in fractured hydrocarbon reservoirs. *Int J Rock Mech Min Sci* 34(3):113-e1.

Gutshall PL, Gross GE (1969) Observations and mechanisms of fracture in polycrystalline alumina. *Eng Fract Mech* 1(3):463-470.

Huang D, Wang J, Liu S (2015) A comprehensive study on the smooth joint model in dem simulation of jointed rock masses. *Granul Matter* 17(6):775-791.

Hoek E, Martin CD (2014) Fracture initiation and propagation in intact rock – A review. *J Rock Mech Geotech Eng* 6:287-300.

Itasca Consulting Group, Inc. UDEC v6.00 Manual, 2010.

Jaeger JC, Cook NG, Zimmerman R (2007) *Fundamentals of Rock Mechanics*. 4th Ed. Wiley-Blackwell.

Jenabidehkordi A (2018) Computational methods for fracture in rocks: a review and recent advances. *Front Struct Civ Eng* 13:273-287.

Justo J, Castro J, Cicero S, Sánchez-Carro MA, Husillos R (2017) Notch effect on the fracture of several rocks: application of the Theory of Critical Distances. *Theor Appl Fract Mech* 90:251-258.

Justo J, Castro J, Cicero S (2018) Energy-based approach for fracture assessment of several rocks containing U-shaped notches through the application of the SED criterion. *Int J Rock Mech Min Sci* 110:306-315.

Justo J, Castro J, Cicero S (2020) Notch effect and fracture load predictions of rock beams at different temperatures using the Theory of Critical Distances. *Int J Rock Mech Min Sci* 125:104161.

Kochen R, Andrade JCO (1997) Predicted behavior of a subway station in weathered rock. *Int J Rock Mech Min Sci* 34(3):160-e1.

Li XF, Li HB, Zhao J (2017) 3D polycrystalline discrete element method (3PDEM) for simulation of crack initiation and propagation in granular rock. *Comput Geotech* 90:96-112.

Liu HZ, Lin JS, He JD, Xie HQ (2018) Discrete elements and size effects. *Eng Fract Mech* 189:246-272.

Moosavi S, Scholtès L, Giot R (2018) Influence of stress induced microcracks on the tensile fracture behavior of rocks. *Comput Geotech* 104:81-95.

Nassir M, Settari A, Wan R (2013) Joint stiffness and deformation behaviour of discontinuous rock. *J Can Petrol Technol* 49(9):78-85.

Neuber H (1958) *Theory of notch stresses: principles for exact calculation of strength with reference to structural form and material*. Springer Verlag, Berlin.

Nicksiar M, Martin CD (2014) Factors affecting crack initiation in low porosity crystalline rocks. *Rock Mech Rock Eng* 47:1165-1181.

Parisio F, Tarokh A, Makhnenko R, Naumov D, Miao XY, Kolditz O, Nagel T (2019) Experimental characterization and numerical modelling of fracture processes in granite. *Int J Solids Struct* 163:102-116.

Peterson RE (1959) Notch sensitivity. In: Sines G, Waisman JL (Eds.), *Metal Fatigue*. McGraw Hill, New York 293–306.

Potyondy DO, Cundall PA (2004) A bonded-particle model for rock. *Int J Rock Mech Min Sci* 41:1329-1364.

Rawlings C, Barton N, Bandis S, Addis M, Gutierrez M (1993) Laboratory and numerical discontinuum modeling of wellbore stability. *J Petrol Tech* 45(11):1-86.

Scholtès L, Donzé FV (2012) Modelling progressive failure in fractured rock masses using a 3D discrete element method. *Int J Rock Mech Min Sci* 52:18-30.

Srawley J, Gross B (1976) Side-cracked plates subject to combined direct and bending forces. *Cracks and Fracture*, ASTM STP 601:559-579.

Susmel L, Taylor D (2003) Fatigue design in the presence of stress concentrations. *Int J Strain Anal Eng Compon* 38:443–452.

Susmel L, Taylor D (2010) An elasto-plastic reformulation of the Theory of Critical Distances to estimate lifetime of notched components failing in the low/medium-cycle fatigue regime. *J Eng Mater Technol Trans ASME* 132:0210021–0210028.

Tarokh A, Fakhimi A (2014) Discrete element simulation of the effect of particle size on the size of fracture process zone in quasi-brittle materials. *Comput Geotech* 62:51-60.

Tarokh A, Makhnenko RY, Fakhimi A, Labuz JF (2017) Scaling of the fracture process zone in rock. *Int J Fract* 204:191-204.

Taylor D, Wang G (2000) The validation of some methods of notch fatigue analysis. *Fatigue Fract Eng Mater Struct* 23:387–394.

Taylor D (2007) *The Theory of Critical Distances: a new perspective in fracture mechanics*. London, Elsevier.

Taylor D (2017) *The Theory of Critical Distances: a link to micromechanisms*. *Theor Appl Fract Mech* 90:228-233.

Timoshenko S, Goodier JN (1951) *Theory of Elasticity*. McGraw Hill.

Wang F, Konietzky H, Herbst M (2019) Influence of heterogeneity on thermo-mechanical behaviour of rocks. *Comput Geotech* 116:103184.

Weiss V (1962) Application of Weibull's statistical theory of fracture to sheet specimens. *Trans ASME* 62-WA-270.

Whittaker BN, Singh RN, Sun G (1992) *Rock fracture mechanics: principles, design, and applications*. Elsevier.

Wong RHC, Chau KT, Wang P (1996) Microcracking and grain size effect in Yuen Long marbles. *Int J Rock Mech Min Sci Geomech* 33(5):479-485.

Yingren Z, Shangyi Z (2004) Application of strength reduction fem in soil and rock slope. *Chin J Rock Mech Eng* 19 037.

Yue L, Sun S, Liu J, Wei J, Wu J (2017) Research on crack initiation mechanism and fracture criterion of rock-type materials under compression-shear stress. *Adv Mech Eng* 9(10):1-13.